RESEARCH ARTICLE

Check for updates

Spray-assisted deposition of a SnO₂ electron transport bilayer for efficient inkjet-printed perovskite solar cells†

Vinayak Vitthal Satale, [ID] [a] Neetesh Kumar, [ID] [a] Hock Beng Lee, [ID] [a]
Manoj Mayaji Ovhal, [ID] [a] Sagnik Chowdhury, [ID] [a] Barkha Tyagi, [ID] [a]
Asmaa Mohamed [ID] [a,b] and Jae-Wook Kang [ID] *[a]

Developing an efficient electron transport layer (ETL) through structural modification is essential to produce high-performance perovskite solar cell (PSC) devices. Specifically, the ETL should exhibit low defects, high optical transparency, and charge selectivity for ideal electron transport. Herein, we demonstrate (i) the low-temperature fabrication of tin oxide (SnO₂) ETLs with a bilayer structure, and (ii) inkjet-printing of triple-cation perovskite films. Through the combined use of spin-coating and spray deposition, the optimized SnO₂-bilayer ETL shows a nano-granule-textured surface, noticeably fewer defects, and a cascade conduction band position with the inkjet-printed perovskite film. The champion PSC device, based on the SnO₂-bilayer ETL and inkjet-printed perovskite film, recorded an outstanding power conversion efficiency (PCE) of ~16.9%, which is significantly higher than the device based on the conventional SnO₂ ETL (PCE ~14.8%). The improved photovoltaic performance of the SnO₂-bilayer-based device arises mainly from more efficient charge transport and suppressed recombination at the ETL/perovskite interface. The SnO₂-bilayer ETL and inkjet-printed perovskite films demonstrated herein can be potentially used for large-scale manufacturing of photovoltaic modules.

1. Introduction

In recent years, the power conversion efficiency (PCE) of lab-scale perovskite solar cells (PSCs) has reached an astoundingly high value of 25.7% by virtue of structural and defect engineering.[1] Conventionally, the perovskite photoabsorber films in PSCs are deposited using one-step antisolvent or two-step sequential deposition methods, both of which rely heavily on the spin-coating process.[2,3] The well-known spin-coating technique relies on centrifugal forces to generate the necessary liquid–vapor interface for perovskite film deposition, and thus, it exhibits poor scalability and limits the commercialization potential of PSCs. Consequently, numerous deposition methods that offer low raw material utilization rates and high film uniformity, such as vacuum deposition,[4] spray deposition,[5] brush painting,[6] doctor-blade coating,[37] and inkjet printing,[7] have been explored for the large-scale preparation of

perovskite films. Among these methods, inkjet printing (IJP) is the most material-efficient technique because it offers high cost-effectiveness, high writing accuracy, and a near-unity material utilization ratio.[8,9] The IJP technique has been popular for fabricating large-area perovskite films with a precisely-controlled thickness and interface, yielding satisfactory performance in planar PSCs.[10] Currently, the highest PCE achieved by inkjet-printed perovskite solar cell (IJP-PSC) is 21.7%, based on the p-i-n type configuration.[11] The IJP technique also allowed the fabrication of PSC devices with all-inkjet-printed perovskite absorbers and charge extraction layers with a maximum PCE of 17.2%.[7] Li *et al.* successfully prepared a large-area PSC device using the IJP technique and achieved a PCE of 18.64%.[12] The overall performance of IJP-PSCs is converging upon the state-of-the-art values achieved by solution-processed PSCs.

In the initial phase of the investigation, TiO₂ as an electron transport layer (ETL) was commonly used in n-i-p structured PSCs owing to its outstanding electronic and optical properties.[13,14] Based on the use of the mesoscopic TiO₂ ETL and inkjet-printed MAPbI₃ perovskite, the PSC achieved a maximum PCE of 12.3%.[15] However, the high processing temperature (>450 °C), low conductivity, and vulnerability to photo-oxidation of the TiO₂ layer make it less desirable for long-term use in PSCs.[13] As a replacement for TiO₂, low-temp-

*a*Department of Flexible and Printable Electronics, LANL-CBNU Engineering Institute-Korea, Jeonbuk National University, Jeonju 54896, Republic of Korea.
E-mail: jwkang@jbnu.ac.kr
*b*Department of Physics, Faculty of Science, South Valley University, Qena 83523, Egypt
†Electronic supplementary information (ESI) available: Experimental, Fig. S1–S5, and Tables S1–S5. See DOI: https://doi.org/10.1039/d3qi00599b

erature processable (<185 °C) ETLs such as ZnO,[16] WO₃,[17] NbO$_x$,[18] CeO$_x$,[38] Fe₂O₃,[19] and SiO₂ [20–22] were introduced and applied in PSCs. In particular, SnO₂ has been investigated extensively due to its highly comparable optoelectronic properties with TiO₂, including high optical transparency and charge selectivity, excellent electron mobility (240 cm² V^{-1} s^{-1}), and more importantly, low-temperature processability.[23] Furthermore, SnO₂ has a favorable energy level alignment with the commonly used FAPbI₃/MAPbI₃ perovskites, *i.e.* having conduction and valence band edges below the perovskite absorber for efficient charge collection and blocking at the ETL/perovskite interfaces.[23]

In its pristine state, solution-processed SnO₂ exhibits a defect-rich nature, which is undesirable for its role as the ETL. To reduce the defect states and enhance the energy band structure, SnO₂ has been used in tandem with other metal oxides, such as TiO₂, to form a bilayer ETL for solution-processed PSC devices, resulting in improved charge extraction and a PCE of ~19.8%.[24] Thereafter, an amorphous-crystalline SnO₂-bilayer with a unique morphology was developed using a low-temperature solution process, further boosting the PCE of PSCs to 20.39% by virtue of improved charge transfer at the SnO₂/perovskite interface.[25] These works have demonstrated the advantages of low-temperature processed bilayer ETLs which leads to the enhanced performance of solution-processed PSCs. In the current stage, the use of the SnO₂ ETL is less popular for IJP-PSCs. Initially, a mesoporous TiO₂ ETL and FAMAPbBr₃ absorber were used to fabricate PSC devices, which showed a good PCE of 14.11%.[26] Also, MAPbI₃ and CsFAMAPb(Br, I)₃-based IJP-PSCs fabricated with TiO₂ as the ETL have achieved maximum PCEs of 18.20% and 19.60%.[12,27] The IJP-PSC devices fabricated with modified compact and mesoporous TiO₂ ETLs exhibited a PCE of 9.1%.[28] To the best of our knowledge, there is only one report demonstrating the use of an SnO₂ ETL for IJP-PSCs, in which a PCE of 10.35% was achieved by incorporating polymer additives into the perovskites.[29] To improve the charge transfer without altering the optical properties of ETLs, the utilization of bilayer ETLs can be a successful strategy for enhancing the device performance of IJP-PSCs.

Here, we rationally designed a highly crystalline SnO₂-bilayer ETL *via* the combined use of spin-coating and spray-deposition approaches. Specifically, a ~30 nm thick SnO₂ underlayer was first deposited on the substrate by spin-coating the sol–gel precursor, followed by the spray deposition of SnO₂ colloidal solution to produce an overlaying scaffold layer. In this individual case, the spin-coated SnO₂ (spin-SnO₂) film exhibits a smooth yet compact surface, whereas the spray-deposited SnO₂ (spray-SnO₂) film has a mesoporous, nanograin-textured surface. Therefore, the resulting SnO₂-bilayer ETL can inherit the exceptional morphological features found in both spin-SnO₂ and spray-SnO₂ films. The characterization confirmed that the SnO₂-bilayer exhibits better morphology, reduced defects, and more suitable conduction and valence band alignments with the inkjet-printed perovskite layer than the commonly used spin-SnO₂. The results show that the SnO₂-bilayer can prevent direct contact among the ITO/perovs-

kite layers more effectively than the spin-SnO₂ and spray-SnO₂ ETLs. At the same time, the SnO₂-bilayer also exhibited a nano-granule-textured surface which produces larger surface-to-volume ratios as compared with spin-SnO₂ and spray-SnO₂ single-layer films, creating a maximum ETL/absorber interfacial area for efficient charge transport. Thus, the best SnO₂-bilayer-based IJP-PSC successfully attained a maximum PCE of 16.9%, and its significantly higher PCE is associated with the spin-SnO₂ based devices. The spray-assisted SnO₂-bilayer ETL developed herein can be potentially used to develop large-scale IJP-PSC devices with improved performance and durability.

2. Results and discussion

2.1 Structural, morphological, and optoelectronic properties of SnO₂ films

The SnO₂-bilayer ETL was fabricated using a two-step strategy, *i.e.* spin coating the sol–gel precursor solution and a spray deposition technique, as demonstrated in Fig. 1(a). The synthesis parameters for spray coating have been applied as mentioned in the previous literature[21] to produce high-quality SnO₂ films. In the digital photographs of the spin-SnO₂, spray-SnO₂, and SnO₂-bilayer films shown in Fig. 1(b), the color of the SnO₂-bilayer film is more greenish than the spin and spray-SnO₂ films. Based on the water contact angle (WCA) profiles displayed in Fig. 1(c), the spray-SnO₂ (θ ~41°) and SnO₂-bilayer (θ ~46°) films showed more hydrophobic behavior than the spin-SnO₂ (θ ~25°) film. As discussed in previous work,[30] the wettability of the substrate or ETL/HTL and the growth of perovskite grains are closely linked. Low-density nuclei are produced on the hydrophobic substrate in the initial nucleation step, and can further expand and coarsen to larger grains during the thermal annealing step. Fig. 1(d) displays the X-ray diffraction (XRD) patterns of the spin-SnO₂, spray-SnO₂, and SnO₂-bilayer films, broad diffraction peaks with lower intensity owing to the ultra-fine size (~3 nm) of SnO₂.[21] The diffraction peaks observed in all the three films at the 2θ values of 26.6°, 33.9°, 38.8°, 51.8°, and 65.91° corresponding to the (110), (101), (200), (211), and (310) planes, respectively. These spectra match well with JCPDS no.: 01-072-1147, confirming the tetragonal crystal structure of tin oxide.[21]

The prepared spin-SnO₂, spray-SnO₂, and SnO₂-bilayer films over glass substrates were used for further studies. The transmittance spectra of all three SnO₂ films were recorded using a UV-visible spectrometer and are shown in Fig. 1(e). The transmittance values at a wavelength of 550 nm for spin-SnO₂, spray-SnO₂, and SnO₂-bilayer films are 96.9%, 96.3%, and 95.6%, respectively, and this trend matches well with previous work.[25] The thickness (obtained from the surface profilometer) of the spin-SnO₂ is ≈30 nm, and that of spray-SnO₂ is ≈60 nm,[21,25] whereas the thickness of the SnO₂-bilayer was quite increased with a value of ≈80 nm. The reduction in the transmittance can be associated with the increased thickness of bilayer-SnO₂ films. The optical band gap (E_g) of the different SnO₂ ETLs was calculated from the Tauc plot (inset) in
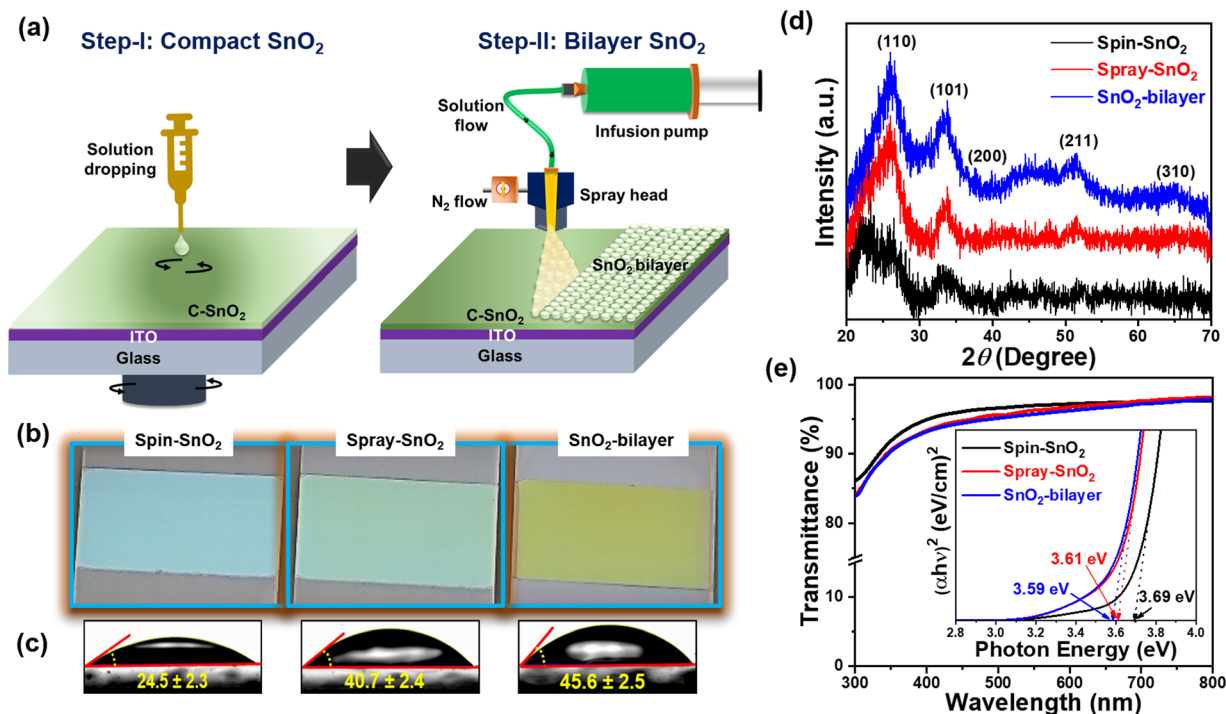
This journal is © the Partner Organisations 2023

Inorg. Chem. Front., 2023, **10**, 3558–3567 | **3559**

Fig. 1 (a) Schematic illustration of the fabrication process of SnO_2-bilayer films, (b) digital photographs of SnO_2 films coated on patterned ITO substrates, (c) contact angles of water on spin-SnO_2, spray-SnO_2, and SnO_2-bilayer films, (d) XRD patterns, and (e) transmittance spectra and the Tauc plot (inset) of spin-SnO_2, spray-SnO_2, and SnO_2-bilayer films.

Fig. 1(e). The obtained E_g values for spin-SnO_2, spray-SnO_2, and SnO_2-bilayer films are ~3.69 eV, ~3.61 eV, and ~3.59 eV, respectively. The small change in E_g is due to the substantial variation in the band alignment of the SnO_2 resulting from surface texture upgradation.

The surface texture of the spin-SnO_2, spray-SnO_2, and SnO_2-bilayer films was investigated using a field-emission scanning electron microscope (FE-SEM). From the FE-SEM images in Fig. 2(a), the spin-SnO_2 film had a compact morphology, whereas the surfaces of spray-SnO_2 and SnO_2-bilayer films were covered with ultrafine granular structures. The average size of the nano-granules in the spray and SnO_2-bilayer films was ~40 nm. These granules on the spray and SnO_2-bilayer film surfaces are also visible through atomic force microscopy (AFM) analysis. The micrographs shown in Fig. 2(b) reveal that these granules were absent on the surface of spin-SnO_2, which confirms that it can be only formed during the *in situ* spray coating process.[21] Their nano-textured-granule structure, spray-SnO_2, and SnO_2-bilayer films exhibited a slightly larger specific root-mean-square (RMS) roughness values of ~2.7 nm and ~2.6 nm compared with spin-SnO_2 (RMS ≈2.1 nm). These ultrafine granules give rise to a mesoporous morphology in the spray-SnO_2 and SnO_2-bilayer films, which can increase the contact area at the interface of the ETL/absorber for efficient charge collection.[21,25]

X-ray photoelectron microscopy (XPS) analysis was performed to study the surface elemental composition of the spin-SnO_2, spray-SnO_2, and SnO_2-bilayer films. Fig. 3a

describes that the O 1s core level spectra of three SnO_2 films were elaborated into different oxygen components, namely O_1, O_2, and O_3. Precisely, the major O_1 peak situated at a lower binding energy (BE) of ≈530 eV is related to the lattice oxygen in the Sn–O, however, the minor O_2 (≈531.5 eV) and O_3 (≈532.5 eV) peaks are correlated with the oxygen vacancies (V_O) and dangling hydroxyl (–OH) groups confined in SnO_2, respectively.[25,31]

The amount of lattice ($O_{lattice}$; O_1) and defects (O_{defect}; $O_2 + O_3$) for oxygen atoms were estimated for all SnO_2 films by calculating the area under the curve for every O component. In Table S1,† it is presented that the spin-SnO_2 film exhibited a larger [$O_{defect}/O_{lattice}$] fraction of ≈0.41, indicating the abundance of oxygen-related defects in the spin-SnO_2 film surface acquired. In contrast, the SnO_2-bilayer film exhibited the lowest fraction of [$O_{defect}/O_{lattice}$] ≈0.28, suggesting that the presence of very few oxygen defects and the O component originates mainly from Sn–O. A lower fraction [$O_{defect}/O_{lattice}$] of the SnO_2-bilayer film initiates mostly from the decrease of –OH groups (O_3). The main reason for the dominant charge transport from the ETL/absorber interface can be related to these –OH groups and V_O defects which create recombination sites on the ETL surfaces. Hence, the knowingly fewer O-defects in the SnO_2-bilayer film are incredibly advantageous for charge transport in PSCs.

Alongside the XPS measurements, UPS measurements were conducted to investigate the energy band alignments of all SnO_2 films. Fig. 3(b–d) present the UPS spectra of the SnO_2
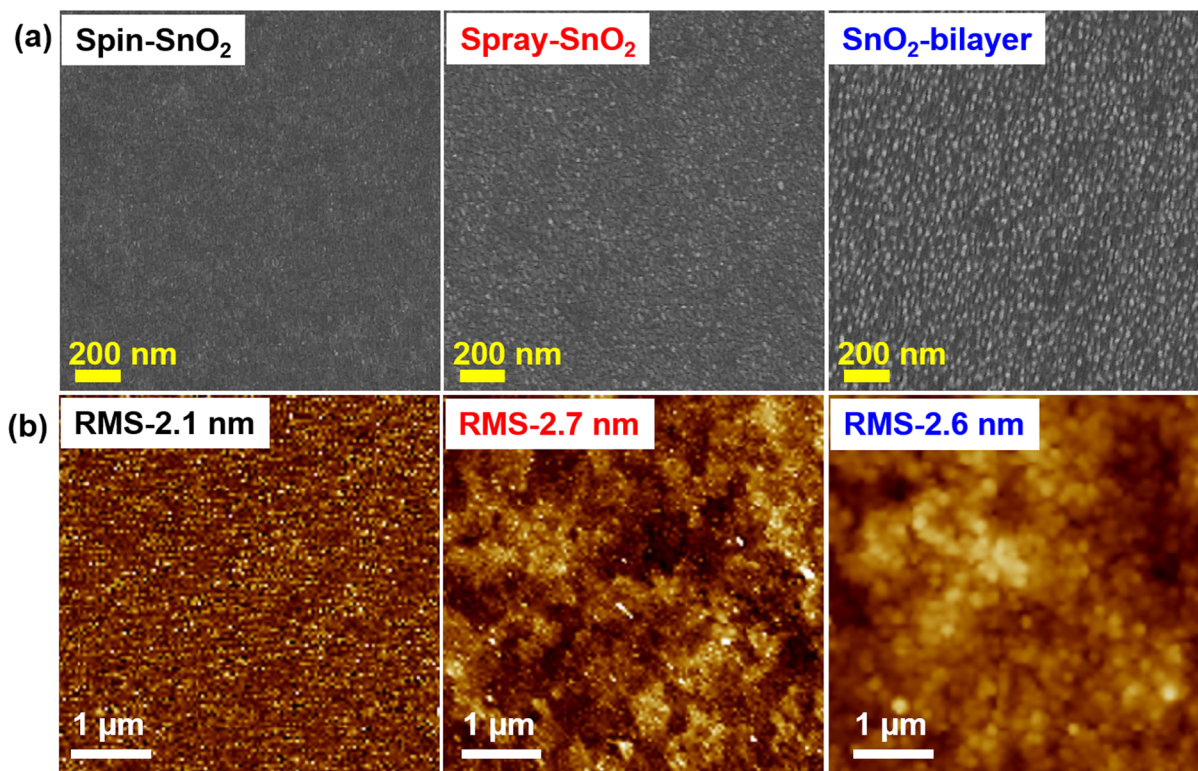
Fig. 2 (a) Top-view FE-SEM images and (b) AFM micrographs depicting the surface morphologies and topographies of spin-SnO_2, spray-SnO_2, and SnO_2-bilayer films.
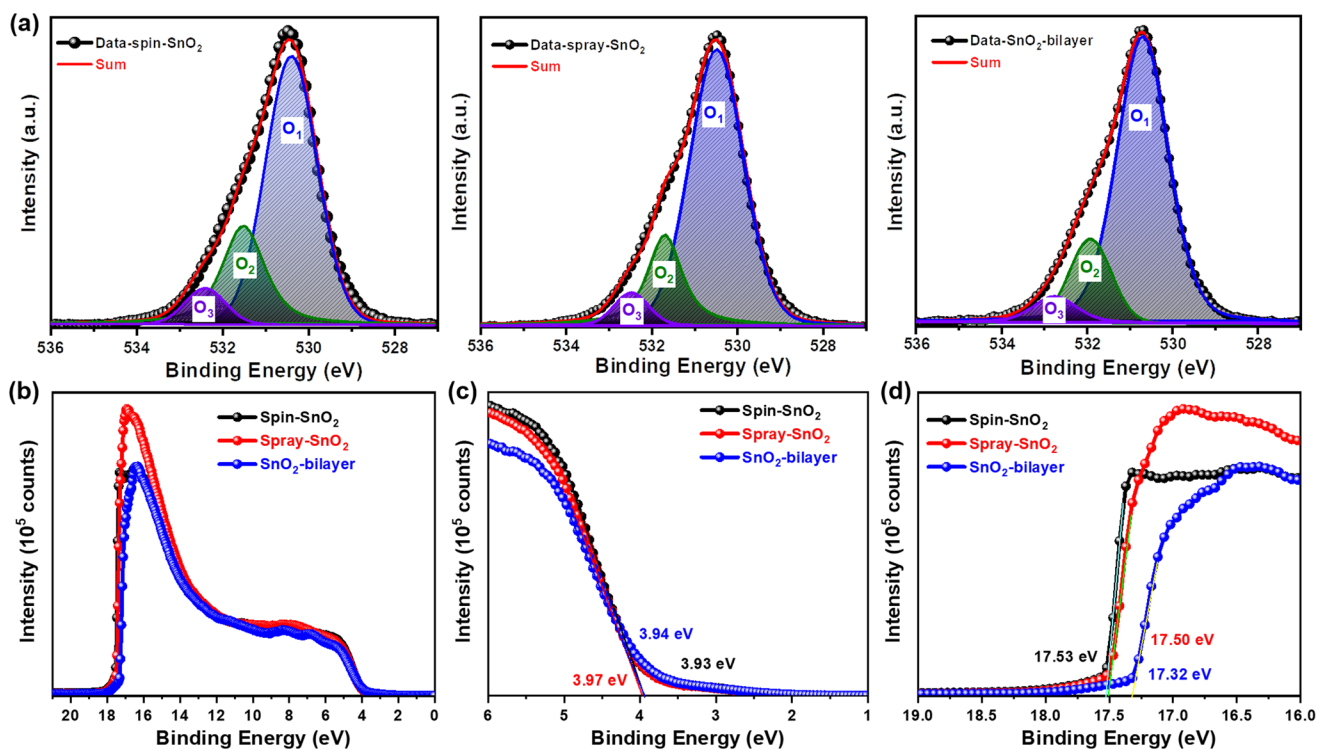

Fig. 3 (a) XPS spectra of the O 1s core level of different SnO_2 films (spin-SnO_2, spray-SnO_2, and SnO_2-bilayer) on ITO glass. (b) Ultraviolet photo-electron spectroscopy (UPS) spectra, (c) on-set region, and (d) cut-off region of spin-SnO_2, spray-SnO_2, and SnO_2-bilayer films.

This journal is © the Partner Organisations 2023

Inorg. Chem. Front., 2023, **10**, 3558–3567 | **3561**

films, cut-off edge, and valence band region. The values of $E_{\text{cut-off}}$ and $E_{\text{on-set}}$ were extracted from Fig. 3(c and d) for all SnO_2 films and are summarized in Table S2.† Using Expression S1,† the work function (W_S) values of the spin-SnO_2, spray-SnO_2, and SnO_2-bilayer films were estimated to be −3.69, −3.72, and −3.90 eV, respectively. Meanwhile, the valence band energy levels (E_{VB}) of the spin-SnO_2, spray-SnO_2, and SnO_2-bilayer films were estimated as −7.62, −7.69, and −7.84 eV, individually (Expression S2†). The calculated conduction band energy level (E_{CB}) values for the spin-SnO_2 (−4.04 eV), spray-SnO_2 (−3.97 eV), and SnO_2-bilayer (−4.11 eV) films reveal the deeper E_{CB} of the SnO_2-bilayer could effectively transfer the electrons from the perovskite to SnO_2. In addition, the deeper E_{VB} of the spray-SnO_2 and SnO_2-bilayer than the spin-SnO_2 possibly will efficiently reduce bimolecular recombination at the SnO_2/absorber interface, which can improve charge transport. The XPS and UPS outcomes taken together verify the alterations in the elemental composition and the exact energy band position of the SnO_2-bilayer ETL can contribute positively to the performance of inkjet-printed photovoltaic devices.

2.2 Structural, morphological, and optoelectronic properties of inkjet-printed perovskite films

Fig. 4(a) schematically illustrates the inkjet-printing process of triple-cation perovskite films on different SnO_2 ETLs. The structural information and crystal phase of the resulting inkjet-printed SnO_2/perovskite films were analyzed using an X-ray diffractometer. Based on the XRD patterns in Fig. 4b, all of the perovskite films displayed a prominent peak corresponding to the (001) plane at a 2θ value of ~14.1° regardless of the SnO_2 underlayers. In addition to the (001) peak, other representative peaks such as (011), (111), (002), (012), (112), (022), and (003) were also detected, which can be indexed to the cubic crystal structure of the $CsFAMAPbBr_xI_{3-x}$ perovskite.[32,33] Comparatively, the intensities of the (001) and (002) planes in the SnO_2-bilayer/perovskite film are relatively higher than those of the spin-SnO_2/perovskite and spray-SnO_2/perovskite samples, implying the superior crystallinity of the perovskite film in the former. A low-intensity subtle peak of the δ-phase[34] perovskite was observed at 11.78° in all three samples, indicating the incomplete transformation of the
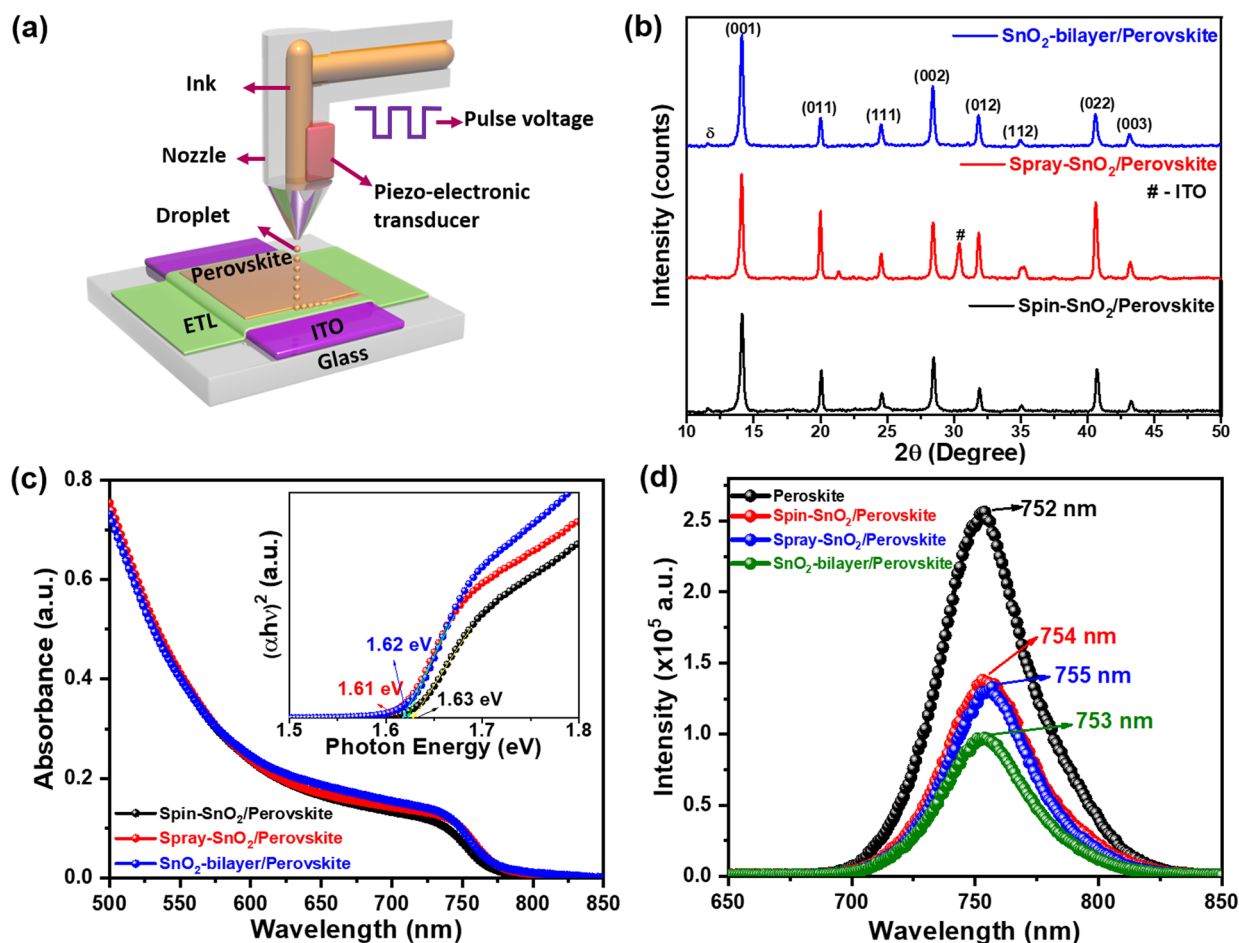

Fig. 4 (a) Schematic illustration of perovskite film fabrication using inkjet printing. (b) X-ray diffraction (XRD) patterns of inkjet-printed perovskite films fabricated on spin-SnO_2, spray-SnO_2, and SnO_2-bilayer ETLs. (c) UV-vis spectra and the Tauc plot (inset) of inkjet-printed perovskite films fabricated on spin, spray, and SnO_2-bilayer ETLs. (d) Steady-state photoluminescence (PL) spectra of inkjet-printed perovskite films fabricated on spin, spray, and SnO_2-bilayer ETLs.

3562 | *Inorg. Chem. Front.*, 2023, **10**, 3558–3567

This journal is © the Partner Organisations 2023

Published on 10 2023. Downloaded on 19-11-24 14.35.18.

δ-phase (yellow) perovskite to the α-phase (black) perovskite.[32] The PbI$_2$ peak was not detected in all of the samples, indicating the formation of highly crystalline perovskite films over different SnO$_2$ underlayers. The estimated crystallite sizes (Debye–Scherrer formula) for the spin-SnO$_2$/perovskite, spray-SnO$_2$/perovskite, and SnO$_2$-bilayer/perovskite samples were calculated to be ~34.5 nm, 36.4 nm, and 36.5 nm, respectively.

Furthermore, all of the SnO$_2$/inkjet-printed perovskite films revealed an absorption edge in the region of 760–770 nm (Fig. 4c), and estimated values of E_g ≈1.63–1.61 eV (inset). Simultaneously, steady-state photoluminescence (PL) results revealed the electron extraction dynamics at the SnO$_2$/perovskite interface, and the resulting PL spectra are displayed in Fig. 4(d). The reference inkjet-printed perovskite film showed pronounced PL emission that peaked at 752 nm. With the spin-SnO$_2$, spray-SnO$_2$, and SnO$_2$-bilayer ETLs, the inkjet-printed perovskite films showed quenching of the intensity by ~46%, ~47%, and ~63%, respectively. Apparently, the SnO$_2$-bilayer can extract the charge more efficiently than the other counterparts at the SnO$_2$/perovskite interface, as evident in its largest PL quench. This is because the SnO$_2$-bilayer exhibited a lower fraction of oxygen defects and –OH groups, which act as trap states. Moreover, the PL spectra also revealed a minor red-shift in the emission peak of the perovskite films using SnO$_2$ ETLs, possibly due to the strain induced by lattice distortion.[35]

The FE-SEM images displayed in Fig. 5a revealed that all inkjet-printed perovskite samples are more compact, pinhole-free, and made up of distinct grains. The grain size distributions of the various SnO$_2$/perovskite films were presented in histogram plots (insets). The SnO$_2$-bilayer/perovskite sample had an average grain size of ≈130 nm, which is larger than the spin-SnO$_2$/perovskite (≈122 nm) and spray-SnO$_2$/perovskite (≈123 nm) samples. The larger grain size is due to the hydrophobic nature of the SnO$_2$ ETL layer, which correlates well with the wettability results of SnO$_2$ ETLs discussed above. The cross-sectional FE-SEM images of the perovskite layers deposited over different SnO$_2$ ETLs are shown in Fig. S1.† The average thickness values for spin-SnO$_2$/perovskite, spray-SnO$_2$/perovskite, and SnO$_2$-bilayer/perovskite samples were found to be ~405, ~395, and ~398 nm, respectively. The AFM micrographs (Fig. S1†) illustrate that the surface of the inkjet-printed perovskite films is denser, without pinholes/voids, and these results are more related to FE-SEM as discussed previously. The values of RMS roughness for the inkjet-printed perovskite film over the spin-SnO$_2$, spray-SnO$_2$, and SnO$_2$-bilayer ETLs was measured to be ~33 nm, ~24 nm and ~21 nm, respectively. The uniform and smooth surface of the inkjet-printed perovskite films can be potentially used for the manufacturing of large-scale semitransparent photovoltaic devices.[36]

The core-level XPS spectra of Pb 4f, I 3d, Br 3d, C 1s, N 1s, and Cs 3d elements of the inkjet-printed perovskite film over glass substrate are shown in Fig. S2(a).† Generally, Pb 4f spectra consist of two high-intensity Pb 4f$_{7/2}$ and Pb 4f$_{5/2}$
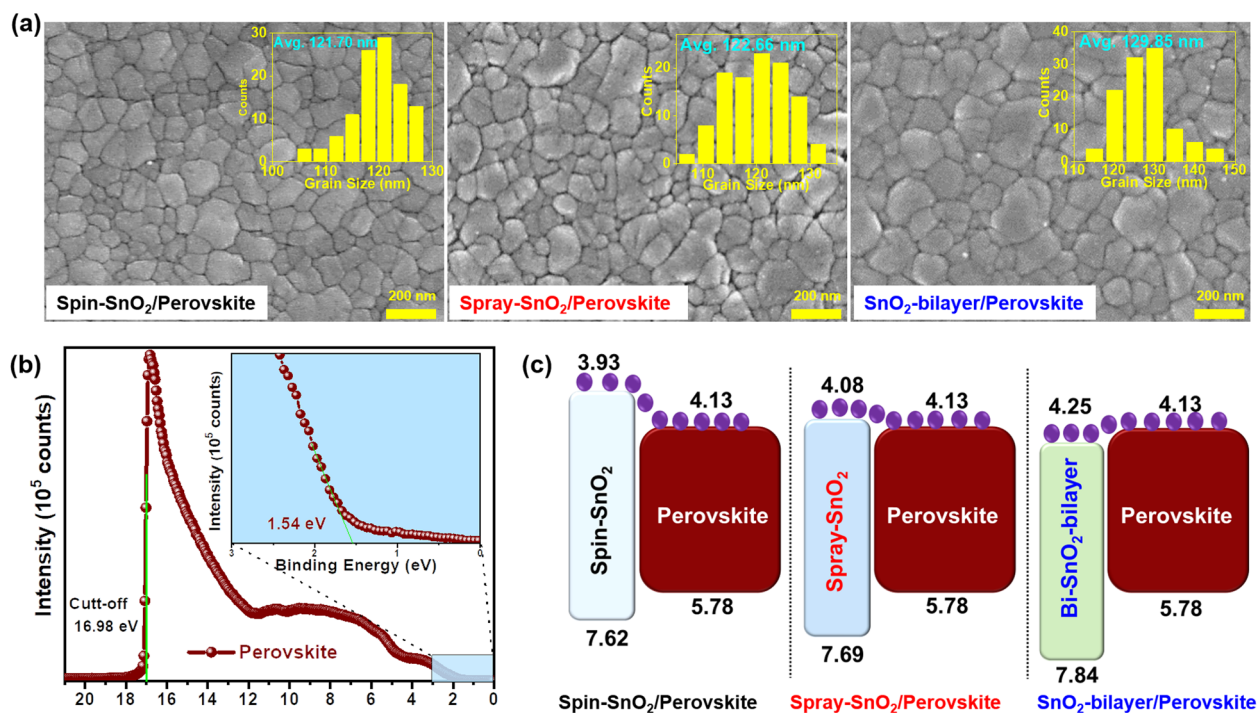

Fig. 5 (a) Surface morphologies and grain size distributions (inset) of perovskite films inkjet-printed on different SnO$_2$ ETLs. (b) Ultraviolet photoelectron spectroscopy (UPS) spectra of the perovskite film; the inset shows the onset region. (c) Schematic energy band alignment of inkjet-printed perovskite films with different SnO$_2$ ETLs.

peaks that exist at BEs of 138.2 and 143.1 eV, respectively, with a spin–orbital splitting of 4.9 eV. The spectrum of I 3d shows two leading peaks at BEs of 619 and 630.5 eV. Fig. S2(b),† corresponding to the I $3d_{5/2}$ and I $3d_{3/2}$ components, individually. Fig. S2(c)† illustrates the two dominant peaks of the Br 3d core level spectrum at BEs of 68.3 and 69.2 eV belonging to the Br $3d_{5/2}$ and Br $3d_{3/2}$, respectively. Similarly, the C 1s and N 1s core-level spectra in Fig. S2(d) and (e)† depict the C=NH_2^+ at 288.04 and 400.28 eV, respectively. The Cs 3d spectrum in Fig. S2(f)† represents the intensity of the Cs $3d_{5/2}$ and Cs $3d_{3/2}$ core levels at 724.5 eV and 738.53 eV, respectively. These results confirmed that the inkjet-printed perovskite film has high phase purity.

The $E_{cut\text{-}off}$ and $E_{on\text{-}set}$ values of the inkjet-printed perovskite film are investigated *via* UPS measurements. The values of work function (W_S), as well as the valence band maximum (E_{VB}) of the inkjet-printed perovskite film, were estimated from Fig. 5b and using Exp. S(1 and 2).† The conduction band maximum (E_{CB}) and band gap values were estimated from Exp. S3† and the Tauc plot, respectively. All these parameters are summarized in Table S2.† The results revealed that the E_{CB} of the SnO₂-bilayer ETL had a smaller band offset with the E_{CB} of the perovskite film, which is more beneficial for collecting charges at the SnO₂/perovskite interface (Fig. 5c). Meanwhile, an energy barrier of ~0.05 eV was seen in the E_{CB} value of the spray-SnO₂ ETL and the E_{CB} value of the perovskite film, which can impede the interfacial electron transfer. The biggest band offset was observed in the spin-SnO₂/perovskite interface, which can cause interfacial recombination of charge carriers and reduce the overall device performance. In addition, the

deeper E_{VB} value of the SnO₂-bilayer compared to the spin-SnO₂ and spray-SnO₂ ETLs can help to inhibit recombination at the SnO₂/perovskite boundaries, thereby improving the device performance of IJP-PSCs. Overall, these results have confirmed that significant variations have arisen in the elemental composition and band alignment of the SnO₂-bilayer/perovskite film, which can lead to considerable changes in the device performance of PSCs.

2.3 Device performance of IJP-PSCs based on different SnO₂ ETLs

To investigate the device performance of SnO₂ ETLs, we fabricated *n-i-p* type IJP-PSCs with a device configuration of ITO/SnO₂/inkjet-printed perovskite/spiro-OMeTAD/Ag, as schematically illustrated in Fig. 6(a). Fig. 6(b) displays the current density and voltage (*J–V*) curves of the representative IJP-PSC devices fabricated on spin-SnO₂, spray-SnO₂, and SnO₂-bilayer ETLs, and the detailed device parameters are presented in Table 1.

Based on the use of a similar inkjet-printed perovskite film, the device made up of a SnO₂-bilayer ETL attained a notably better PCE of ~16.9% compared to the devices based on spin-SnO₂ (PCE ~14.8%) and spray-SnO₂ (PCE ~15.3%) ETLs. The superior performance of the SnO₂-bilayer-based IJP-PSCs is mostly related to the efficient charge transfer between the SnO₂/perovskite layers. Suitable band alignment and improved charge transfer at the ETL/perovskite interface can enhance the V_{oc} and FF of the device. SnO₂-bilayer-based devices recorded a higher FF of 77.73% compared to those based on spin-SnO₂ (FF: 70.56%) and spray-SnO₂ (FF: 70.64%). A similar
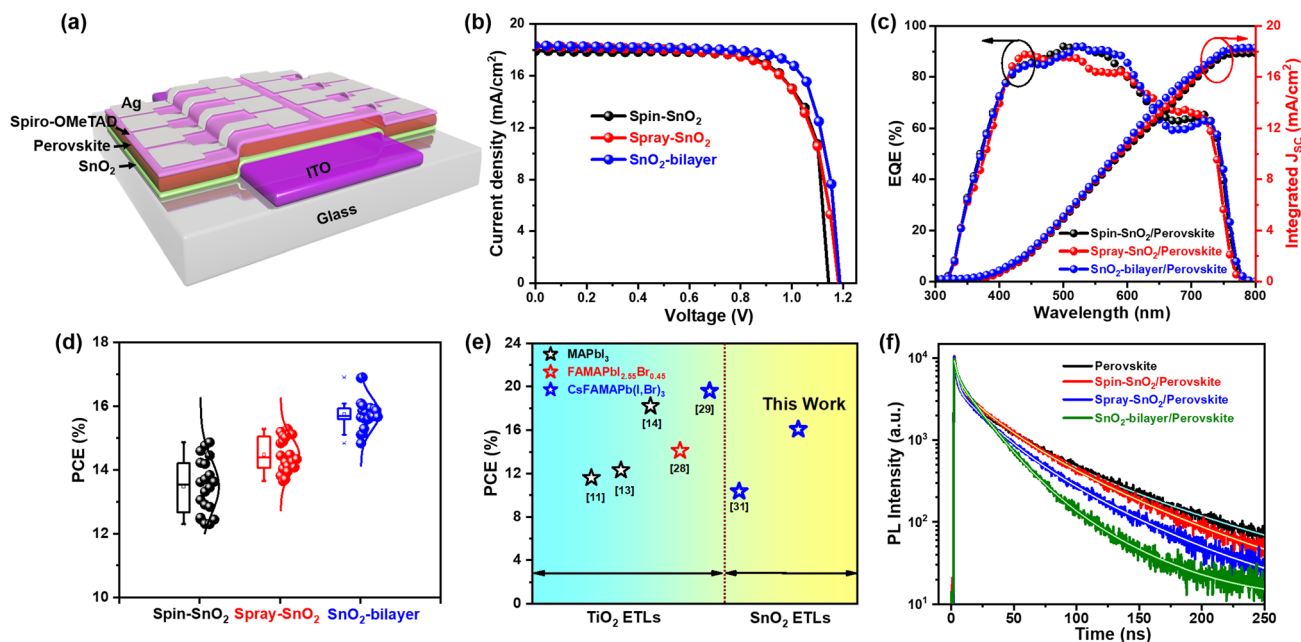

Fig. 6 (a) Schematic device architecture of a complete PSC device. (b) *J–V* characteristic curves, (c) EQE spectra and integrated photocurrent density of PSC devices based on different SnO₂ ETLs and inkjet-printed perovskite films. (d) PCE distributions of inkjet-printed PSCs based on different SnO₂ ETLs. (e) Comparison of the performance of state-of-the-art IJP-PSCs based on TiO₂ and SnO₂ ETLs. (f) TRPL spectra of inkjet-printed perovskite films coated on different SnO₂ ETLs.

3564 | *Inorg. Chem. Front.*, 2023, **10**, 3558–3567

This journal is © the Partner Organisations 2023

Table 1 Photovoltaic performance of inkjet-printed PSCs based on different SnO$_2$ ETLs

Device	V_{oc} [V]	J_{sc} [mA cm^{-2}]	J_{sc} (EQE) [mA cm^{-2}]	FF [%]	PCE [%]	Avg. PCE [%]
Spin-SnO$_2$	1.168	17.92	17.89	70.56	14.77	13.48 ± 0.8
Spray-SnO$_2$	1.182	18.31	18.21	70.64	15.29	14.49 ± 0.5
SnO$_2$-bilayer	1.187	18.32	18.30	77.73	16.90	15.76 ± 0.5

improvement was observed in the V_{oc} of the SnO$_2$-bilayer-based device (V_{oc}: 1.187 V) compared to the devices based on spin-SnO$_2$ (V_{oc}: 1.168 V) and spray-SnO$_2$ (V_{oc}: 1.182 V). The higher V_{oc} of the SnO$_2$-bilayer-based device is attributable to the deeper E_{VB} of the SnO$_2$-bilayer ETL relative to those of the spin-SnO$_2$ and spray-SnO$_2$ ETLs. Overall, in the literature, the PCE of our IJP-PSC devices is the highest amongst the SnO$_2$-based inkjet-printed PSC systems, as shown in Fig. 6(e).[10,12,13,26,27,29] The literature survey of the performance of IJP-PSC photovoltaic devices based on different TiO$_2$ and SnO$_2$ ETLs is presented in Table S5.† To provide further insight, electro-optical characterization was performed on IJP-PSC devices. The integrated J_{sc} values of the devices were estimated from the external quantum efficiency (EQE) spectra in Fig. 6(c). The device based on the SnO$_2$-bilayer exhibited an integrated J_{sc} value of 18.30 mA cm^{-2}, which matches well with the measured J_{sc} values obtained from the J–V measurement (Table 1). On another note, we also investigated the long-term stability and photostability of IJP-PSC devices comprising different SnO$_2$. The photostability measurements showed that all three devices generated stable J_{sc} values over a prolonged one-sun illumination for 500 s (Fig. S5(a)†). Nonetheless, the shelf-life of the IJP-PSCs based on spin-SnO$_2$ and spray-SnO$_2$ was lower than the analogues based on the SnO$_2$-bilayer (Fig. S5(b)†). Moreover, the performance of 20 IJP-PSC devices with different SnO$_2$ ETLs was tested, and confirmed reproducibility data were displayed in a PCE distribution plot in Fig. 6(d). Among all, IJP-PSCs based on the SnO$_2$-bilayer ETL achieved the highest average PCE of (15.76 ± 0.5)%, which clearly shows the highly reproducible performance of the devices. The J–V curves of IJP-PSC devices under forward-scan and reverse-scan are shown in Fig. S4,† and the hysteresis index (HI) of every device was calculated using Expression S4.† The IJP-PSC device made with a SnO$_2$-bilayer showed a considerably lower HI (~0.001) compared with the spin-SnO$_2$ (~0.012) and spray-SnO$_2$ (~0.007), and these low HI values were attributed to the improved SnO$_2$ ETL/perovskite interfacial morphology.[25] Furthermore, we fabricated normal PSC devices based on spin-coated perovskite films and tested them under similar conditions. The forward and reverse scan J–V curves are depicted in Fig. S3,† and estimated J–V parameters are described in Table S3.† Using the same SnO$_2$-bilayer ETL, the PCE of the inkjet-printed PSC device (~16.9%) only showed an ~0.3% PCE decrease from that of the spin-coated PSC (PCE ~17.2%). Meanwhile, the devices made with spin-SnO$_2$ and spray-SnO$_2$ showed considerably larger PCE deficit values of ~2.4% and ~1.9%. This finding shows that the SnO$_2$-

bilayer is a better ETL for IJP-PSCs, and it can also be flexibly used in solution-processed PSCs with different perovskite systems to produce good performance.

To study the charge transport properties between the SnO$_2$ ETL and the inkjet-printed perovskite absorber, we performed transient photoluminescence (TRPL) measurements on the SnO$_2$/perovskite films, and the fluorescence decay lifetimes (τ_{PL}) of the samples were estimated using Expression S5.† As presented in Fig. 6(f), the reference inkjet-printed perovskite film (without SnO$_2$) showed the maximum τ_{PL} of 54 ns. With the incorporation of SnO$_2$-bilayer, the τ_{PL} values of the inkjet-printed perovskite film decreased to 25 ns (Table S4†), signifying a highly effective charge transfer at the SnO$_2$/perovskite interface that contributed positively to the device performance of IJP-PSCs.

3. Conclusion

In summary, we have successfully developed SnO$_2$-bilayer ETLs with better uniformity and a granule-textured surface using a solution-processed spin/spray-coating technique. The SnO$_2$-bilayer ETL displayed a pinhole free nanograin-textured surface that benefitted the printing of the larger grain perovskite overlayer compared with spin-SnO$_2$ and spray-SnO$_2$ films. The device performance of SnO$_2$-bilayer and spray-SnO$_2$ ETLs was investigated using the spin-SnO$_2$ ETL as a reference. The IJP-PSCs made with the SnO$_2$-bilayer ETL and inkjet-printed perovskite film exhibited superior performance with a PCE of ~16.9%, compared to those of the spin-SnO$_2$ (PCE ~14.8%) and spray-SnO$_2$ (~15.3%) analogues. The spray-assisted deposition of SnO$_2$ ETLs and the inkjet-printing of perovskite films under ambient conditions enable the production of large-area photovoltaic devices/modules that are entirely compatible with roll-to-roll (R2R) processing over rigid/flexible electrodes.

Author contributions

V. V. S.: conceptualization, visualization, methodology, formal analysis, investigation, and writing – original draft, review and editing. N. K.: methodology, supervision and writing – review and editing. H. B. L.: supervision and writing – review and editing. M. M. O.: methodology, writing – review and editing, and formal analysis. S. C.: methodology and formal analysis. B. T.: methodology and formal analysis. A. M.: formal analysis. J.-W. K.: supervision, funding acquisition, and writing – review and editing.

Conflicts of interest

The authors declare no conflict of interest.

Acknowledgements

References

1 H. Min, D. Y. Lee, J. Kim, G. Kim, K. S. Lee, J. Kim, M. J. Paik, Y. K. Kim, K. S. Kim, M. G. Kim, T. J. Shin and S. Il Seok, Perovskite solar cells with atomically coherent interlayers on SnO_2 electrodes, *Nature*, 2021, **598**, 444–450.

2 N. J. Jeon, H. Na, E. H. Jung, T. Y. Yang, Y. G. Lee, G. Kim, H. W. Shin, S. Il Seok, J. Lee and J. Seo, A fluorene-terminated hole-transporting material for highly efficient and stable perovskite solar cells, *Nat. Energy*, 2018, **3**, 682–689.

3 M. M. Lee, J. Teuscher, T. Miyasaka, T. N. Murakami and H. J. Snaith, Efficient hybrid solar cells based on meso-superstructured organometal halide perovskites, *Science*, 2012, **338**, 643–647.

4 J. Feng, Y. Jiao, H. Wang, X. Zhu, Y. Sun, M. Du, Y. Cao, D. Yang and S. F. Liu, High-throughput large-area vacuum deposition for high-performance formamidine-based perovskite solar cells, *Energy Environ. Sci.*, 2021, **14**, 3035–3043.

5 J. E. Bishop, C. D. Read, J. A. Smith, T. J. Routledge and D. G. Lidzey, Fully spray-coated triple-cation perovskite solar cells, *Sci. Rep.*, 2020, **10**, 1–8.

6 J. W. Lee, S. I. Na and S. S. Kim, Efficient spin-coating-free planar heterojunction perovskite solar cells fabricated with successive brush-painting, *J. Power Sources*, 2017, **339**, 33–40.

7 F. Schackmar, H. Eggers, M. Frericks, B. S. Richards, U. Lemmer, G. Hernandez-Sosa and U. W. Paetzold, Perovskite solar cells with all-inkjet-printed absorber and charge transport layers, *Adv. Mater. Technol.*, 2021, **6**, 2000271.

8 B. J. De Gans, P. C. Duineveld and U. S. Schubert, Inkjet printing of polymers: State of the art and future developments, *Adv. Mater.*, 2004, **16**, 203–213.

9 M. Kuang, L. Wang and Y. Song, Controllable printing droplets for high-resolution patterns, *Adv. Mater.*, 2014, **26**, 6950–6958.

10 Z. Wei, H. Chen, K. Yan and S. Yang, Inkjet printing and instant chemical transformation of a $CH_3NH_3PbI_3$/nanocarbon electrode and interface for planar perovskite solar cells, *Angew. Chem., Int. Ed.*, 2014, **53**, 13239–13243.

11 H. Eggers, F. Schackmar, T. Abzieher, Q. Sun, U. Lemmer, Y. Vaynzof, B. S. Richards, G. Hernandez-Sosa and U. W. Paetzold, Inkjet-printed micrometer-thick perovskite solar cells with large columnar grains, *Adv. Energy Mater.*, 2020, **10**, 1903184.

12 P. Li, C. Liang, B. Bao, Y. Li, X. Hu, Y. Wang, Y. Zhang, F. Li, G. Shao and Y. Song, Inkjet manipulated homo-geneous large size perovskite grains for efficient and large-area perovskite solar cells, *Nano Energy*, 2018, **46**, 203–211.

13 T. Leijtens, G. E. Eperon, S. Pathak, A. Abate, M. M. Lee and H. J. Snaith, Overcoming ultraviolet light instability of sensitized TiO_2 with meso-superstructured organometal tri-halide perovskite solar cells, *Nat. Commun.*, 2013, **4**, 1–8.

14 W. Ke, G. Fang, J. Wang, P. Qin, H. Tao, H. Lei, Q. Liu, X. Dai and X. Zhao, Perovskite solar cell with an efficient TiO_2 compact film, *ACS Appl. Mater. Interfaces*, 2014, **6**, 15959–15965.

15 S. G. Li, K. J. Jiang, M. J. Su, X. P. Cui, J. H. Huang, Q. Q. Zhang, X. Q. Zhou, L. M. Yang and Y. L. Song, Inkjet printing of $CH_3NH_3PbI_3$ on a mesoscopic TiO_2 film for highly efficient perovskite solar cells, *J. Mater. Chem. A*, 2015, **3**, 9092–9097.

16 J. Ma, Z. Lin, X. Guo, L. Zhou, J. Su, C. Zhang, Z. Yang, J. Chang, S. (Frank) Liu and Y. Hao, Low-temperature solution-processed ZnO electron transport layer for highly efficient and stable planar perovskite solar cells with efficiency over 20%, *Sol. RRL*, 2019, **3**, 1900096.

17 C. Chen, Y. Jiang, Y. Wu, J. Guo, X. Kong, X. Wu, Y. Li, D. Zheng, S. Wu, X. Gao, Z. Hou, G. Zhou, Y. Chen, J. M. Liu, K. Kempa and J. Gao, Low-temperature-processed WO_x as electron transfer layer for planar perovskite solar cells exceeding 20% efficiency, *Sol. RRL*, 2020, **4**, 1–8.

18 C. Zhang, Y. Shi, S. Wang, Q. Dong, Y. Feng, L. Wang, K. Wang, Y. Shao, Y. Liu and S. Wang, Room-temperature solution-processed amorphous NbO_x as an electron transport layer in high-efficiency photovoltaics, *J. Mater. Chem. A*, 2018, **6**, 17882–17888.

19 Q. Luo, H. Chen, Y. Lin, H. Du, Q. Hou, F. Hao, N. Wang, Z. Guo and J. Huang, Discrete Iron(III) oxide nanoislands for efficient and photostable perovskite solar cells, *Adv. Funct. Mater.*, 2017, **27**, 1–9.

20 A. P. Muthukrishnan, J. Lee, J. Kim, C. S. Kim and S. Jo, Low-temperature solution-processed SnO_2 electron transport layer modified by oxygen plasma for planar perovskite solar cells, *RSC Adv.*, 2022, **12**, 4883–4890.

21 K. Neetesh, H. B. Lee, R. Sahani, B. Tyagi, S. Cho, J.-S. Lee and J.-W. Kang, Room-temperature spray deposition of large-area SnO_2 electron transport layer for high performance, stable $FAPbI_3$-based perovskite solar cells, *Small Methods*, 2022, **6**, 2101127.

22 H. B. Lee, M.-K. Jeon, N. Kumar, B. Tyagi and J.-W. Kang, Boosting the efficiency of SnO_2-triple cation perovskite system beyond 20% using nonhalogenated antisolvent, *Adv. Funct. Mater.*, 2019, **29**, 1903213.

23 J. Xie, K. Huang, X. Yu, Z. Yang, K. Xiao, Y. Qiang, X. Zhu, L. Xu, P. Wang, C. Cui and D. Yang, Enhanced electronic properties of SnO_2 via electron transfer from graphene quantum dots for efficient perovskite solar cells, *ACS Nano*, 2017, **11**, 9176–9182.

24 Y. Lee, S. Paek, K. T. Cho, E. Oveisi, P. Gao, S. Lee, J. S. Park, Y. Zhang, R. Humphry-Baker, A. M. Asiri and M. K. Nazeeruddin, Enhanced charge collection with passi-

3566 | *Inorg. Chem. Front.*, 2023, **10**, 3558–3567

This journal is © the Partner Organisations 2023

vation of the tin oxide layer in planar perovskite solar cells, *J. Mater. Chem. A*, 2017, **5**, 12729–12734.

25 H. B. Lee, N. Kumar, M. M. Ovhal, Y. J. Kim, Y. M. Song and J.-W. Kang, Dopant-free, amorphous–crystalline heterophase SnO_2 electron transport bilayer enables >20% efficiency in triple-cation perovskite solar cells, *Adv. Funct. Mater.*, 2020, **30**, 2001559.

26 A. J. Huckaba, O. Lee, R. Xia, S. Paek, V. C. Bassetto, E. Oveisi, A. Lesch, S. Kinge, P. J. Dyson, H. Girault and N. M. Khaja, Inkjet-printed mesoporous TiO_2 and perovskite layers for high efficiency perovskite solar cells, *Energy Technol.*, 2019, **7**, 317–324.

27 Z. Li, P. Li, G. Chen, Y. Cheng, X. Pi, X. Yu, D. Yang, L. Han, Y. Zhang and Y. Song, Ink engineering of inkjet printing perovskite, *ACS Appl. Mater. Interfaces*, 2020, **12**, 39082–39091.

28 A. Verma, D. Martineau, S. Abdolhosseinzadeh, J. Heier and F. Nüesch, Inkjet printed mesoscopic perovskite solar cells with custom design capability, *Mater. Adv.*, 2020, **1**, 153–160.

29 C. S. Pathak, G. Paramasivam, F. Mathies, K. Hirselandt, V. Schröder, O. Maus, J. Dagar, C. Klimm, E. Unger and I. Visoly-Fisher, PTB7 as an Ink-additive for spin-coated versus inkjet-printed perovskite solar cells, *ACS Appl. Energy Mater.*, 2022, **5**, 4085–4095.

30 J. Chung, S. S. Shin, K. Hwang, G. Kim, K. W. Kim, D. S. Lee, W. Kim, B. S. Ma, Y.-K. Kim, T.-S. Kim and J. Seo, Record-efficiency flexible perovskite solar cell and module enabled by a porous-planar structure as an electron transport layer, *Energy Environ. Sci.*, 2020, **13**, 4854.

31 H. B. Lee, R. T. Ginting, S. T. Tan, C. H. Tan, A. Alshanableh, H. F. Oleiwi, C. C. Yap, M. H. H. Jumali and M. Yahaya, Controlled defects of fluorine-incorporated ZnO nanorods for photovoltaic enhancement, *Sci. Rep.*, 2016, **6**, 1–11.

32 L. Q. Xie, L. Chen, Z. A. Nan, H. X. Lin, T. Wang, D. P. Zhan, J. W. Yan, B. W. Mao and Z. Q. Tian, Understanding the cubic phase stabilization and crystallization kinetics in mixed cations and halides perovskite single crystals, *J. Am. Chem. Soc.*, 2017, **139**, 3320–3323.

33 H. Eggers, F. Schackmar, T. Abzieher, Q. Sun, U. Lemmer, Y. Vaynzof, B. S. Richards, G. Hernandez-Sosa and U. W. Paetzold, Inkjet–printed micrometer–thick perovskite solar cells with large columnar grains, *Adv. Energy Mater.*, 2020, **10**, 1903184.

34 H. B. Lee, N. Kumar, V. Devaraj, B. Tyagi, S. He, R. Sahani, K.-J. Ko, J.-W. Oh and J.-W. Kang, Trifluoromethyl-group bearing, hydrophobic bulky cations as defect passivators for highly efficient, stable perovskite solar cells, *Sol. RRL*, 2021, **5**, 2100712.

35 T. I. Alanazi, O. S. Game, J. A. Smith, R. C. Kilbride, C. Greenland, R. Jayaprakash, K. Georgiou, N. J. Terrill and D. G. Lidzey, Potassium iodide reduces the stability of triple-cation perovskite solar cells, *RSC Adv.*, 2020, **10**, 40341–40350.

36 B. Tyagi, H. B. Lee, N. Kumar, W. Y. Jin, K. J. Ko, M. M. Ovhal, R. Sahani, H. J. Chung, J. Seo and J. W. Kang, High-performance, large-area semitransparent and tandem perovskite solar cells featuring highly scalable a-ITO/Ag mesh 3D top electrodes, *Nano Energy*, 2022, **95**, 106978.

37 A. S. Marques, R. M. Faria, J. N. Freitas and A. F. Nogueira, Low-Temperature Blade-Coated Perovskite Solar Cells, *Ind. Eng. Chem. Res.*, 2021, **60**, 7145–7154.

38 X. Wang, L.-L. Deng, L.-Y. Wang, S.-M. Dai, Z. Xing, X.-X. Zhan, X.-Z. Lu, S.-Y. Xie, R.-B. Huang and L.-S. Zheng, Cerium oxide standing out as electron transport layer for efficient and stable perovskite solar cells processed in lowtemperature, *J. Mater. Chem. A*, 2017, **5**, 1706–1712.

This journal is © the Partner Organisations 2023

Inorg. Chem. Front., 2023, **10**, 3558–3567 | **3567**